21, rue d'Artois, F-75008 PARIS
http : //www.cigre.org

CIGRE US National Committee
2023 Grid of the Future Symposium

Electric Field Grading Design and Validation Tests of a Composite Insulated Cross-arm

Usama AHMED*, Yanlin LI, Favad JANJUA
Shemar Power
Canada

SUMMARY

Composite insulated cross-arms are subjected to high electric field stresses in compact line or retrofit upgrading applications. In this work, the design process and performance verification of electric field grading devices for a 240 kV double Vee composite insulated cross-arm is reported. Finite element method simulations were employed for parametric optimization of cross-arm grading devices that concurrently considered various points of interests. Three-phase service condition and single-phase laboratory test environment was simulated and analyzed. Corona extinction voltage test and water droplet induced corona test were performed verifying that grading devices can effectively control the electric fields on the cross-arm metallic hardware, conductor suspension fittings as well as on the composite insulator housings and triple point seals.

KEYWORDS

Composite cross-arms, composite insulators, corona, electric field, insulated cross-arms

usama@shemar.us

I. Introduction

Today composite insulators are seen as a mature alternative to traditional ceramic insulators and offer indispensable advantages such as slim design, light weight, high bending strength and hydrophobicity. Within the broader composite insulator domain, the application of composite insulated cross-arms (CICA) has gained rising attention in order to meet the demands of building new compact transmission lines in narrow corridors and for upgrading of existing infrastructure [1].

Amongst various other technical aspects, effective control of electric field distribution and magnitude with the help of optimized grading devices is crucial for long term performance and reliability of composite insulated cross-arms. Unfortunately, the hydrophobic behavior of composite insulators which causes moisture to form beads on the housing and imparts them the desirable enhanced performance in polluted environments also makes them more susceptible to the effects of high electric fields. Under wet conditions, the local enhancement of electric field on the boundary of water droplet, air and insulator housing can cause the phenomenon of water droplet induced corona [2] which is recognized as an ageing mechanism for composite insulators. Long-term exposure of water droplet induced corona can lead to loss of hydrophobicity and deterioration of the composite insulators. In addition, excessive surface electric field on metallic insulator fittings and associated hardware can also lead to the generation of corona discharges, with accompanying undesirable effects of radio interference and audible noise. Corona discharges on metallic components can also negatively affect the nearby composite insulator housing.

When composite insulated cross-arms are involved, the issue of high electric field stress is further exacerbated, presenting some additional and unique challenges:

- Insulated cross-arms are invariably applied in compact transmission lines where phases are in a much closer proximity and therefore effect of adjacent phases on the resulting electric field stress is more pronounced. For a given operating voltage, the insulators in compact transmission lines are exposed to higher electric field stresses.

- With the use of insulated cross-arms, the shielding provided by the metallic cross-arms of traditional support structures is absent. In conventional line design configurations, this shielding effect helps to somewhat isolate the subject insulator from the electric field enhancement effects of nearby phases.

- A composite insulated cross-arm presents a more complex geometry requiring bespoke and tailored grading devices that can meet the needs of fitting into tight spaces, ensuring ease of installation and replacement, be aesthetic and of compacted size so as to satisfy the in-situ dry arcing distances without unnecessary increase in the length of cross-arm insulators.

- A composite insulated cross-arm also features more points of interests (POI) where the electric field needs to be analyzed and concurrently graded. These include, the triple points and housings of both the composite suspension and line post insulator(s), the metallic connector node, link fittings, corona and shielding rings as well as the conductor attachment hardware.

Investigation of electrical field distribution of high voltage composite insulator arrangements has been an important topic of interest for the transmission industry [3]. Some studies on electric field computation and grading on different types of composite insulated cross-arms have been presented in [4] – [12]. However, most of these papers focus on numerical simulation alone without carrying out sufficient and direct benchmarking of simulation results with laboratory tests. Moreover, these studies also mostly ignore the modeling and evaluation of conductor attachment fittings which can affect the electric field distribution on the insulated cross-arms and need to be considered simultaneously in order to holistically design and optimize the electric field grading system of the full insulated cross-arm assembly.

In this work the electric potential and field distribution of a 240 kV double Vee composite insulated cross-arm for a suspension structure application has been evaluated using the finite element method (FEM). Extensive simulations were performed for both a service model (three-phase) and laboratory model (single-phase). Primarily, the three-phase simulation model with representative tower structure and line geometry was used to parametrically optimize the size, geometry and positioning of different grading devices.

Additional requirement of power arc protection was considered and an integrated protection ring was designed which combines the function of field grading and arc protection into one compact device thus avoiding superfluous increase in cross-arm length. Detailed representation of the full insulated cross-arm assembly including the twin-bundle conductor suspension hardware was made and size of cross-arm shielding ring was adjusted to get the required field grading effect on the conductor suspension clamps and fittings – thereby omitting the need for a local or dedicated grading device for them.

In addition, single-phase simulations were carried out, both with detailed and simplified representation of the laboratory environment in order to predict the performance of the cross-arm in laboratory tests. Corona extinction voltage, radio interference voltage and water droplet induced corona tests were performed on complete insulated cross-arm assembly alongwith conductor bundle suspension hardware and subsequent comparisons of the obtained test results with the output of single-phase laboratory simulations were carried out.

II. Simulation Set-up and Parameters

3-D model of the 240 kV suspension lattice steel tower with composite insulated cross-arms is shown in Figure 1. In this application only the bottom phases are retrofitted with insulated cross-arms (installed symmetrically on both sides) for ground clearance improvement, whilst the top and middle phases retain the original steel cross-arms and insulator assembly. The total height of the tower is 42 m and the bottom phases with insulated cross-arm are located at a height of 25.5 m above the ground. The horizontal length of the insulated cross-arm is 3.2 m which is identical to the top-phase steel cross-arm while the middle phase steel cross-arm is displaced further outwards with a horizontal length of 4.7 m.

Figure 2 shows the detailed representation of the insulated cross-arm assembly with a double Vee configuration. The insulated cross-arm is comprised of composite line post insulators acting as compression members, composite suspension insulators acting as tension members, connection hardware, grading devices and a suspension fitting string for the conductor bundle. The metallic node provides a focal point where insulator members and the conductor bundle are connected together on the high voltage side.

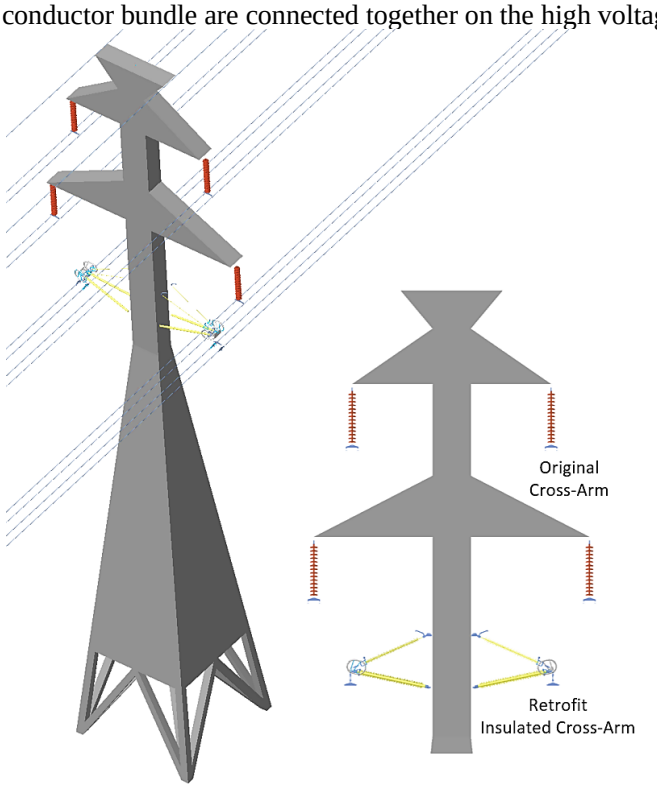

Figure 1. 3-D model of tower with composite insulated cross-arm on bottom phases.

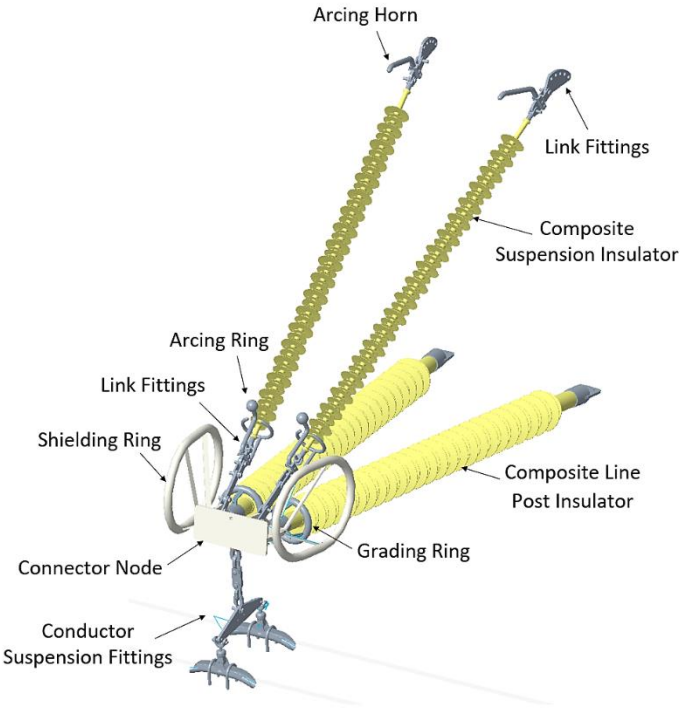

Figure 2. Detailed representation of double Vee composite insulated cross-arm.

The post and suspension insulator both feature a solid fiber reinforced plastic (FRP) core rod which is encapsulated with a high temperature vulcanized (HTV) silicone rubber housing through a vacuum injection molding process. The triple point of the suspension insulator has an over-molded type design whereas the triple point of the post insulator has a sealing ring structure. Primary dimensions of the cross-arm insulators are presented in Table 1. The conductor bundle has twin 20.15 mm diameter sub-conductors with 457 mm horizontal spacing. Suspension fitting string for the conductor is composed of shackles, extension links, yoke plate and suspension clamp with a total length of 700 mm to provide a specified alleviation effect in case of a longitudinal loading event.

Table 1. Main dimensions and mechanical ratings of composite cross-arm insulators

Type	Core Diameter (mm)	Length (mm)	Mechanical Rating
Line Post Insulator	90	2770	20 kN SCL
Suspension Insulator	18	2510	120 kN SML

In the FEM simulations, the service model of the tower, insulated cross-arm and phase conductors were enclosed in an air domain. The dimension of the cuboid simulating the air domain was set to be large enough (35 m x 35 m x 45 m) to maintain accuracy while avoiding unnecessary increase in calculation time. Additionally, due to their minimal impact on the precision of results and to make an optimized use of computational resources, the following simplifications and assumptions were adopted:

- On the double circuit transmission line, the adjacent circuit was not modeled.
- Overhead shield wires were ignored.
- The lattice steel tower was modelled by a fully solid body.
- Traditional suspension insulators for middle and top phases were not modeled.
- Surfaces of the insulated cross-arm were assumed to be dry and clean.

All features of the insulated cross-arm assembly including the conductor suspension fittings were modelled in detail with special attention paid to the detailing of insulator triple points and hardware at the high voltage

end. All edges and corners of the metallic hardware were rounded with their actual radii of curvature. The applied meshing composed of tetrahedral elements was manually optimized with a mesh convergence study which aimed at minimizing the meshing error. Refined meshing with minimum element size of 0.005 mm and maximum element size of 2 mm was used on points of interest of the insulated cross-arm as shown in Figure 3. The total simulation, including domain meshing (71,368,893 elements) and solution computation took approximately 2.5 hours using a computer with Intel Xeon Gold 5218R Processor and 256 GB RAM.

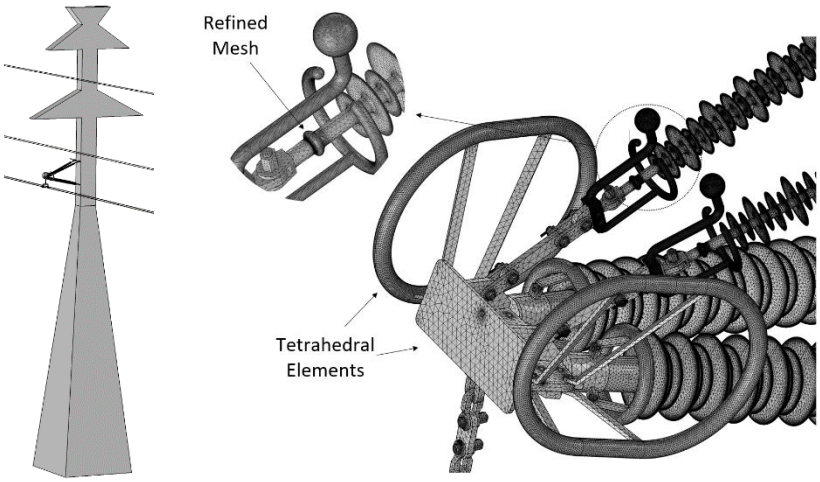

Figure 3. Three-phase service model and refined mesh on points of interest of composite insulated cross-arm.

Stationary electro-static physics was adopted for electric field calculations. The studied (bottom) phase and all metallic hardware of the insulated cross-arm at the high voltage side was assigned a voltage boundary condition of $1.1*240/\sqrt{3} \cong 153$ kV and considering a phase shift of 120°, the adjacent middle and top phase were assigned a voltage of -77 kV. All metallic hardware of the insulated cross-arm on the low voltage side, the tower body and the ground plane were given a potential of 0 V. The relative electric permittivity of different materials used in calculation are listed in Table 2.

Table 2. Electrical permittivity of materials

Component	Material	Permittivity (ε_r)
Insulator sheds and sheath	HTV Silicone Rubber	2.6
Insulator core	FRP	5.0
Insulator end fittings	Steel/Aluminum	1.0
Cross-arm node	Steel	1.0
Grading devices	Steel/Aluminum	1.0
Conductor fittings	Steel/Aluminum	1.0
Cuboid	Air	1.0

It is clarified that metals are not dielectric materials and they are defined in the model by the boundary condition (potential) assigned to them. A default value of 1.0 relative electrical permittivity was used for the metallic elements to fulfil the requirements of the computational algorithm in the FEM software.

Maximum permissible electric field thresholds proposed by EPRI and STRI [13] were adopted as the governing guidelines for design and optimization of insulating cross-arm grading system. These limits are:

- Electric field on insulator triple point seals ≤ 3.5 kV_{rms}/cm
- Electric field on insulator housing over a distance of 10 mm ≤ 4.2 kV_{rms}/cm
- Electric field on metallic hardware and electric field grading devices ≤ 18 kV_{rms}/cm

All calculated electric field strengths are expressed in kV_{rms}/cm.

III. Calculation Results and Optimization of Grading Devices

A. Simulation Results Without Electric Field Grading

In order to identify the specific stress points on the insulated cross-arm, simulations were first carried out without consideration of any electric field grading devices. The resulting potential and electric field distribution on the cross-arm are shown in Figure 4. It can be observed that the potential drop across the cross-arm insulators is highly non-uniform and the electric field stress is largely concentrated on the high voltage side. The maximum evaluated electric field on the housing of suspension and line post insulators, at the high voltage side are 20.80 kV/cm and 8.83 kV/cm respectively which are higher than the specified limits by a considerable margin. Similarly, the resulting strength of electric field on the metallic hardware and fittings at the high voltage end also exceeds the desired threshold. Such high electric fields would result in the formation of corona and thus require application of grading devices. On the low voltage side, the strength of electric field on the insulator housings remains below 3.5 kV/cm, indicating that these points do not need additional field grading. Table 3 provides a summary of the magnitudes of electric field on key points of interest on the insulated cross-arm.

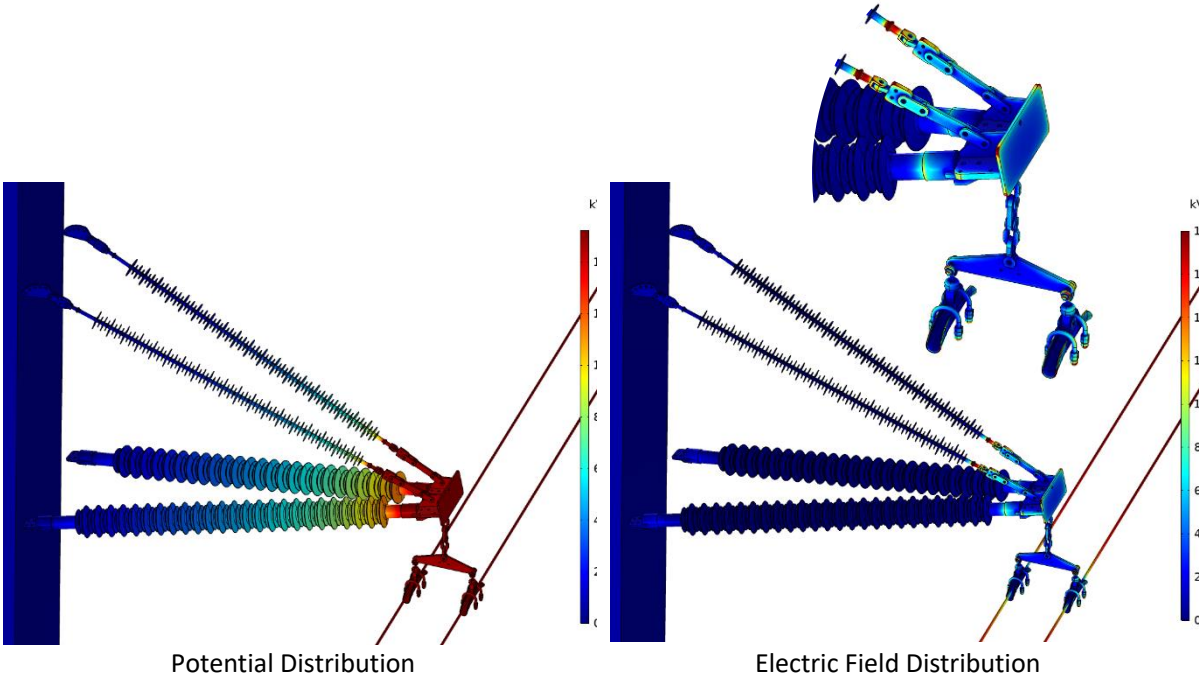

Figure 4. Potential and electric field distribution of insulated cross-arm without grading devices.

Table 3. Maximum electric field strength on insulated cross-arm without grading devices

Potential	Point of Interest	Maximum Electric Field (kV/cm)
High Voltage	Suspension insulator housing	20.80
	Suspension insulator triple point	13.92
	Line post insulator housing	8.83
	Line post insulator triple point	11.02
	Node and hardware	32.18
	Conductor suspension fittings	23.96
Low Voltage	Suspension insulator housing	2.09
	Suspension insulator triple point	1.35
	Line post insulator housing	2.21
	Line post insulator triple point	2.49

B. Conceptualization and Optimization of Grading Devices

Keeping in view the preliminary results of field distribution on the insulated cross-arm, individual grading rings are used to provide a localized electric field stress relief on the composite insulator housings. In addition, shielding rings mirrored on both the left and right side of the high voltage connector node are also

applied to grade the electric field on the metallic hardware and conductor suspension fittings and to improve the overall potential distribution across the cross-arm. To satisfy power arc current withstand requirements, the grading ring of suspension insulator was converted into an integrated arcing ring where the ring provides necessary field grading effect and the protruding leg with an arcing sphere directs and controls the burning of the arc, taking it away from the vulnerable composite insulator. No grading devices were required for the low voltage end of the cross-arm insulator since the electric field at these points is already below the guideline values. The optimization process of the high voltage grading devices was aimed at minimizing the size and manufacturing costs of the grading hardware whilst keeping the electric field at the critical points of interest of the cross-arm below the respective guideline stresses. The final sizing of the grading devices was carried out after taking into account the theoretical minimum dimensions and practical considerations of manufacturer's experience, risk aversion during laboratory testing and actual service, as well as standardization of hardware sizes.

The critical regions or points of interest for the suspension insulator arcing ring are designated as POI-1 to POI-4 and depicted in Figure 5. Based on practical experience, inventory and manufacturing constraints, the following dimensions and structural parameters of the suspension insulator arcing ring were studied:

A – Installation Height: 120, 150, 180, 210 and 240 mm
B – Leg Diameter: 26 mm (determined by arc current withstand)
C – Arcing Sphere Off-set: 183, 193 and 203 mm
D – Tube Diameter: 16, 18, 20 and 22 mm
E – Arcing Sphere Diameter: 60, 65, 70 and 75 mm
F – Ring Outer Diameter: 160, 180, 200 and 220 mm

Numerous electric field simulations were carried out for the 240 kV composite insulated cross-arm wherein one parameter was varied at a time while the other parameters were kept constant.

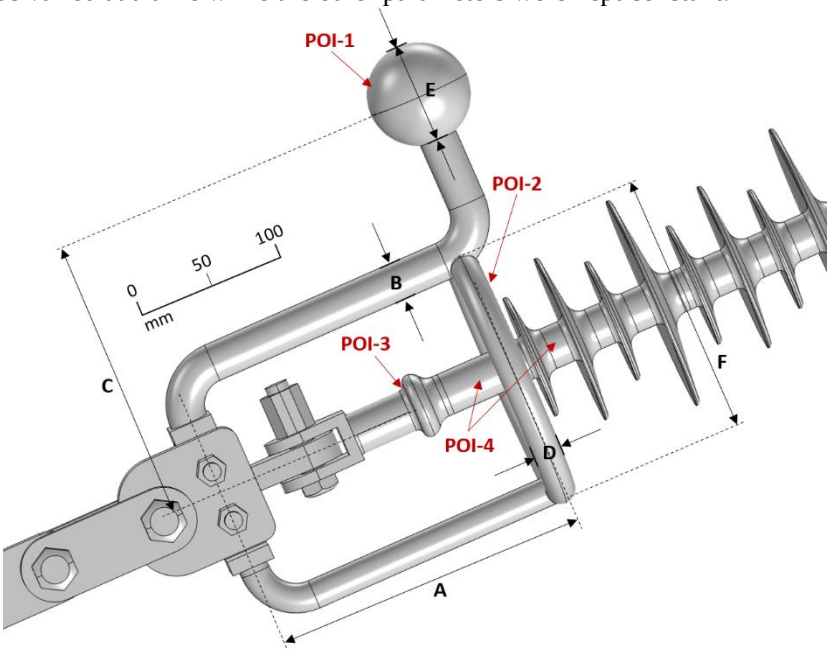

Figure 5. Points of interest and design parameters of suspension insulator arcing ring.

Figure 6 and Figure 7 show the maximum electric field (E_{max}) on the arcing ring surface (POI-2) versus design parameters of the arcing ring. It is apparent that larger ring tube diameter (D) and ring outer diameter (F) result in lower electrical field on its surface. Both Figure 6 and Figure 7 display a marked linear increase in E_{max} with installation height of arcing ring (A).

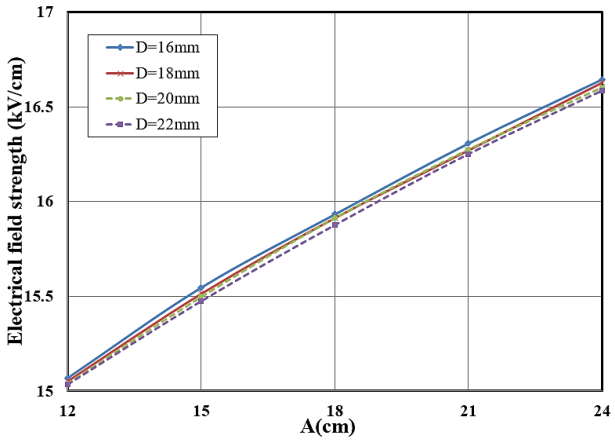

Figure 6. E_{max} on POI-2 (F = 200 mm)

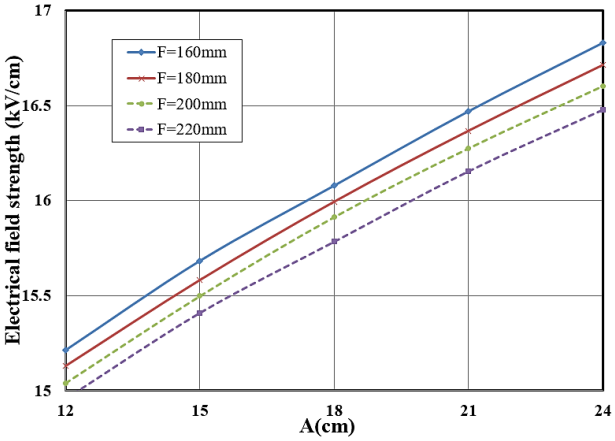

Figure 7. E_{max} on POI-2 (D = 20 mm)

Figure 8 and Figure 9 illustrate E_{max} on the suspension insulator over-molded triple point (POI-3) versus installation height of arcing ring (A). It can be seen that larger tube diameter (D) decreases the electric field however, a larger outer ring diameter (F) can unfavorably increase the electric field stress on POI-3. Both Figure 8 and Figure 9 show that E_{max} decreases at first and then starts to increase at parameter A equal to 18 to 21 cm which can be concluded to be the optimal installation height of the arcing ring with respect to electrical field stress.

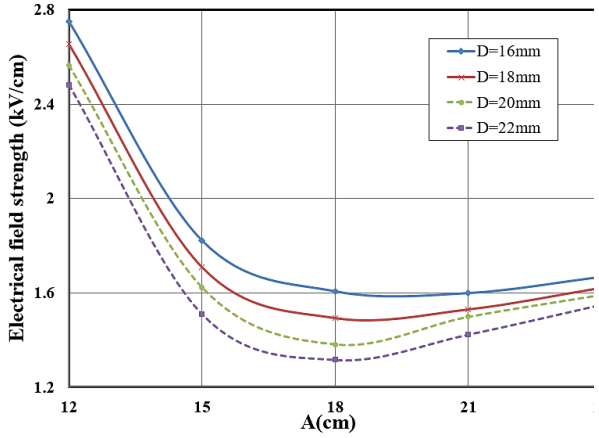

Figure 8. E_{max} on POI-3 (F = 200 mm)

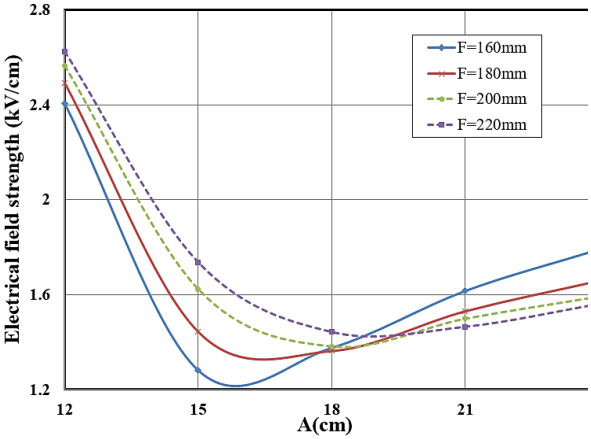

Figure 9. E_{max} on POI-3 (D = 20 mm)

Variation of E_{max} on the suspension insulator sheath and sheds i.e., housing (POI-4) is presented in Figure 10 and Figure 11. Consistent with trend observed before, an increase in parameter D decreases the E_{max} on this point of interest. It can also be seen that beyond installation height of A equal to 18 to 21 cm, the curves are mostly flat and there is no substantial decrease in the electric field strength.

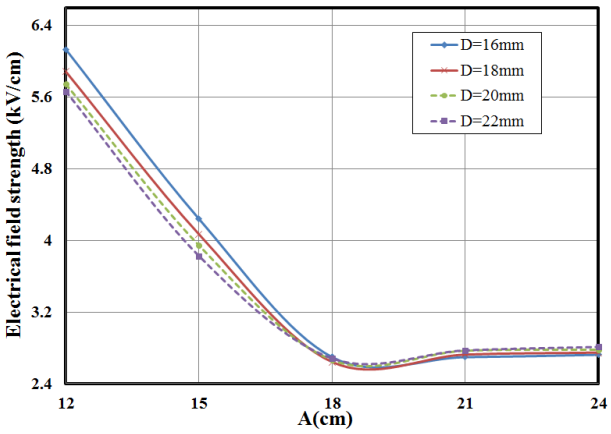

Figure 10. E_{max} on POI-4 (F = 200 mm)

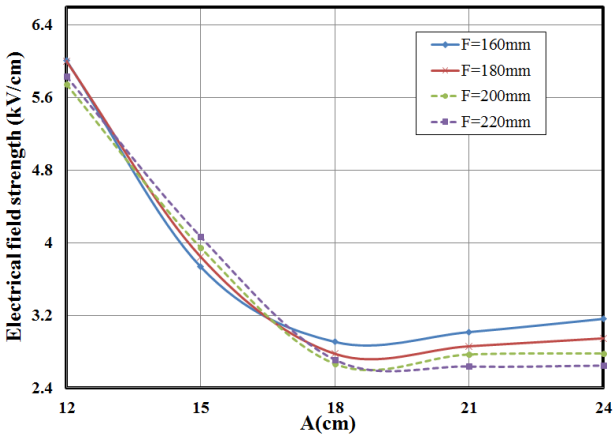

Figure 11. E_{max} on POI-4 (D = 20 mm)

Finally, Figure 12 illustrates E_{max} on arcing sphere (POI-1) versus arcing sphere off-set (C) and sphere diameter (E). The curves illustrated that larger sphere diameter and smaller offset decreases the E_{max} on this region.

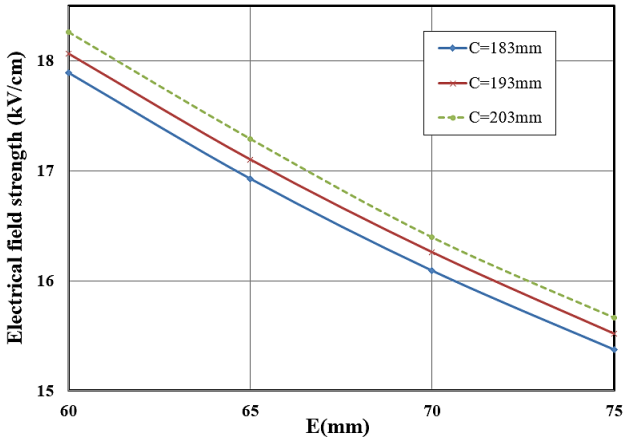

Figure 12. E_{max} on POI-1 (A = 210 mm, D = 20 mm, F = 200 mm)

Based on the preceding analysis, the optimal dimensions of the suspension insulator arcing ring were selected as: A = 210, B = 26, C = 193, D = 20, E = 70 and F = 200 (all in mm). The optimal design of grading ring for composite line post insulators of the cross-arm were also determined following the same procedure with dimensions of 280 mm installation height, 43 mm tube diameter and 200 mm outer ring diameter. These dimensions of grading rings were then used in the subsequent optimization study of the node and conductor hardware shielding ring.

Points of interest for the optimization of shielding ring are labeled as POI-5 to POI-7 and are shown in Figure 13. The following dimensions and structural parameters of shielding ring were studied:

G – Tube Diameter: 40, 50, 60 and 70 mm
H – Installation Height: 410, 435 and 460 mm
I – Shielding Ring Diameter: 470, 500, 530, 560 and 590 mm
J – Length of Straight Section: 200 mm (constant)
K – Installation Off-set: 255 mm (constant)

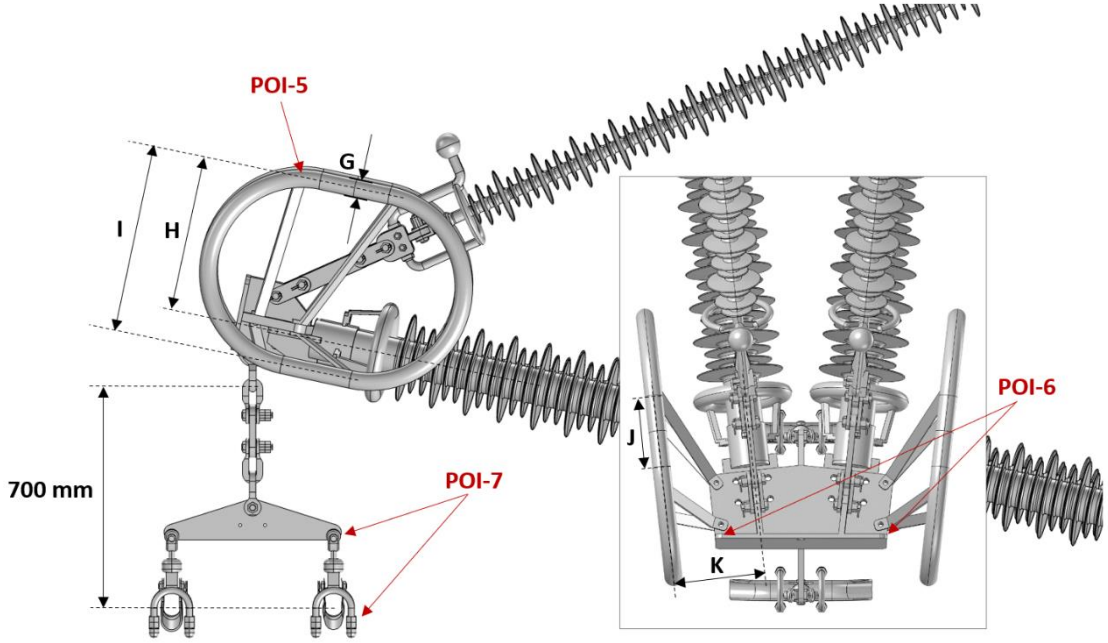

Figure 13. Points of interest and design parameters of insulated cross-arm shielding ring.

Figure 14 and Figure 15 presents the trend of E_{max} on arcing sphere (POI-1) and Figure 16 and Figure 17 illustrate the variation of E_{max} on shielding ring surface (POI-5) versus shielding ring dimensions. It is clear that larger shielding tube diameter and ring diameter (G) contributes to the decrease of electric field stress on these points. It can also be observed that larger installation height (H) leads to smaller E_{max} on POI-1 but greater E_{max} on POI-5.

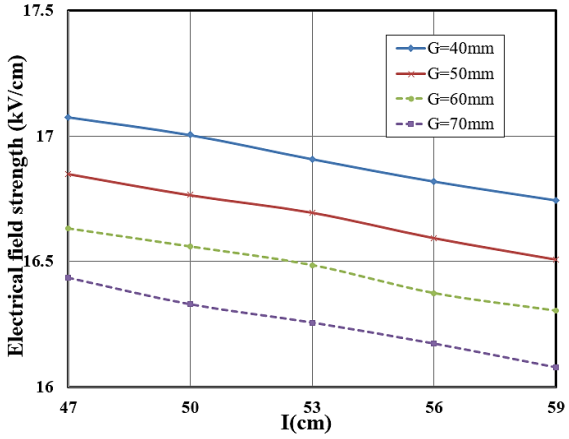

Figure 14. E_{max} on POI-1 (H = 410 mm)

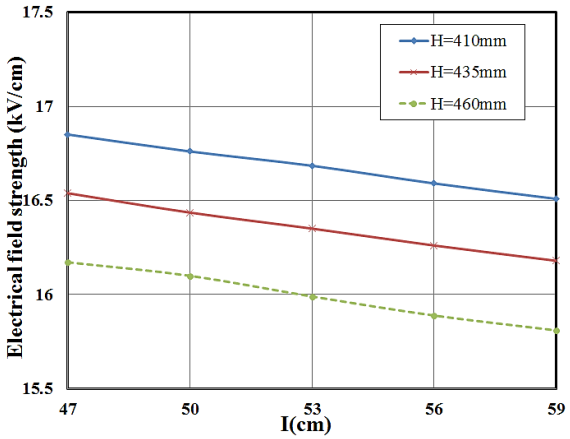

Figure 15. E_{max} on POI-1 (G = 50 mm)

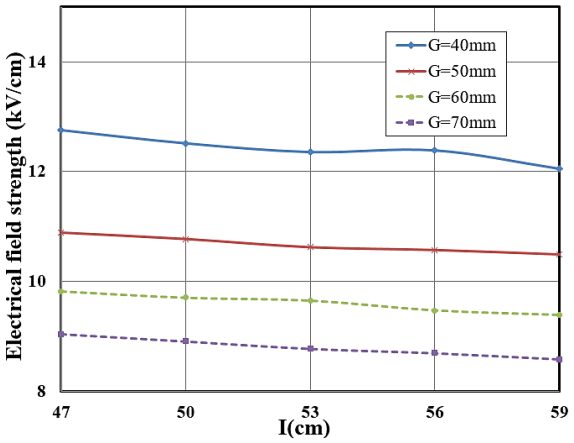

Figure 16. E_{max} on POI-5 (H = 410 mm)

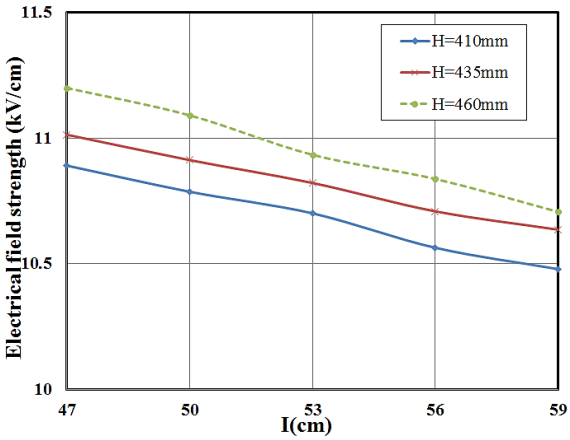

Figure 17. E_{max} on POI-5 (G = 50 mm)

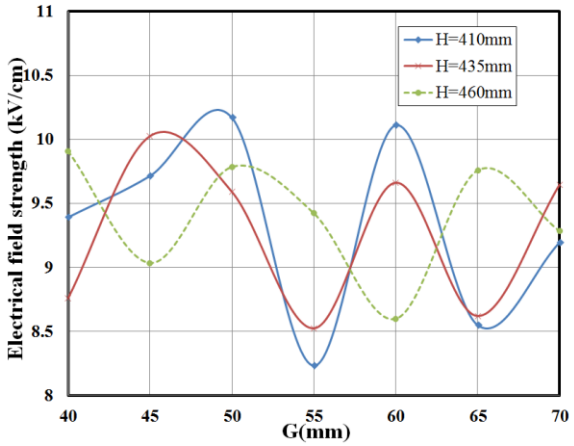

Figure 18. E_{max} on POI-6 (I = 530 mm)

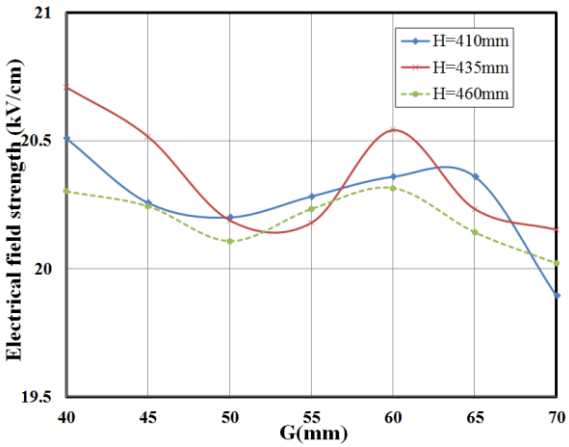

Figure 19. E_{max} on POI-7 (I = 530 mm)

The trend of electric field variation on metallic hardware (POI-6 and POI-7) with respect to shielding ring design parameters as shown in Figure 18 and Figure 19, is less defined and conclusive. Following the above parametric study on shielding ring dimensions, its optimal design was defined as: G = 50, H = 435, I = 530, J = 200 and K = 255 (all in mm).

C. Simulation Results with Grading Devices

The potential and electric field distribution of the insulated cross-arm with optimized grading devices is shown in Figure 20 and the maximum field strength on selected points of interest are provided in Table 4. It can be observed that highest electric field stress regions are concentrated on the surface of the grading devices and the insulator housings, seal points and other metallic hardware and fitting are well shielded. Except the conductor suspension hardware which has sharp curvatures, the maximum electric field strength is observed on the arcing spheres of the suspension insulator with a value of 16.05 kV/cm.

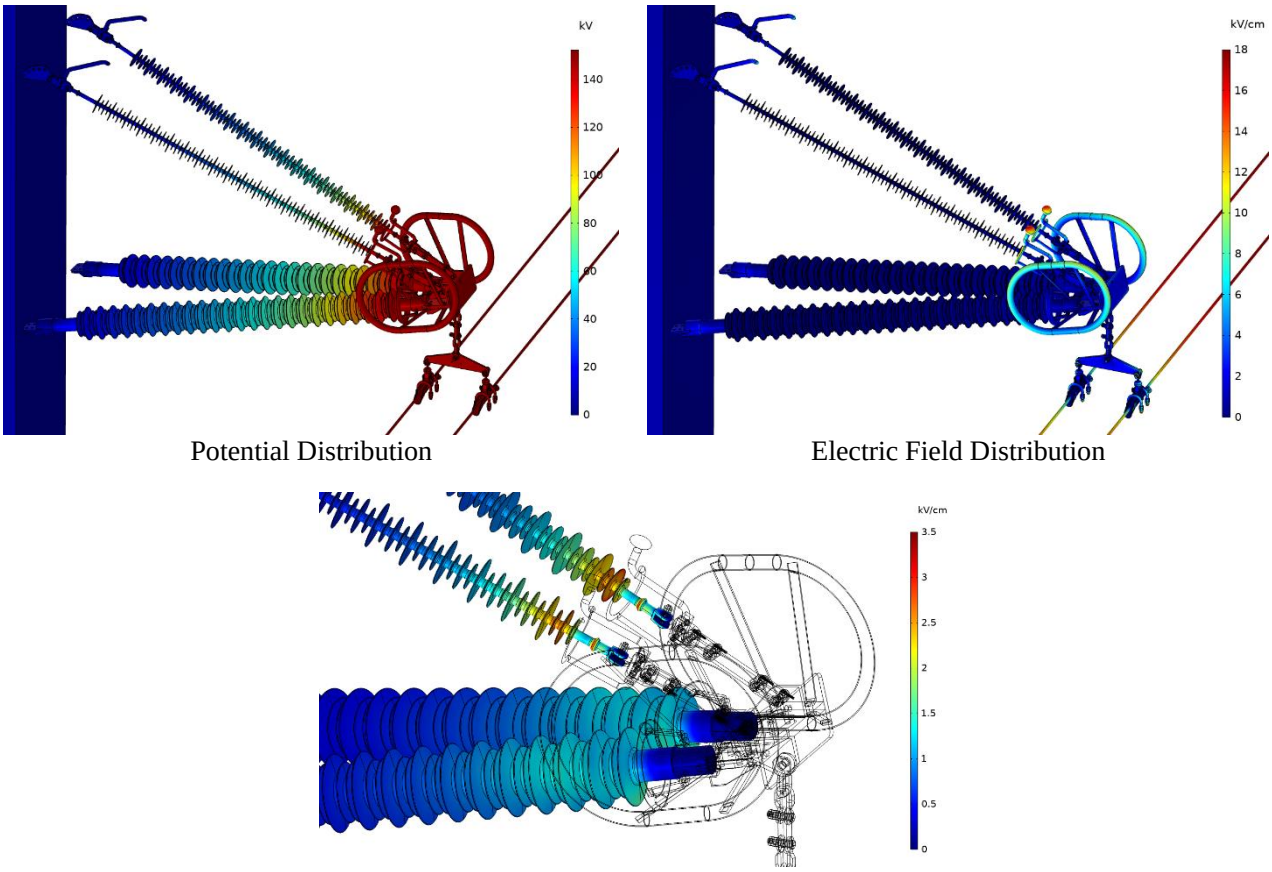

Potential Distribution

Electric Field Distribution

Electric Field Distribution (insulator housing)

Figure 20. Potential and electric field distribution of insulated cross-arm with grading devices

Table 4. Maximum electric field strength on insulated cross-arm with grading devices

Potential	Point of Interest	Maximum Electric Field (kV/cm)
High Voltage	Suspension insulator housing	3.23
	Suspension insulator triple point	1.45
	Line post insulator housing	1.74
	Line post insulator triple point	1.19
	Node and hardware	9.14
	Conductor suspension fittings	19.39
	Node shielding ring	10.62
	Line post insulator grading ring	4.70
	Suspension insulator arcing ring	16.05
Low Voltage	Suspension insulator housing	2.40
	Suspension insulator triple point	1.47
	Line post insulator housing	2.71
	Line post insulator triple point	2.73
	Suspension insulator arcing horn	6.34

The grading effect on the insulators can be better visualized through Figure 21 which compares the potential and electric field distribution along the line post and suspension insulator of the cross-arm, with and without grading devices. It is apparent that with grading devices the potential drop across the insulation is less un-

even exhibiting an improvement of 128 % and 243 % for the first 500 mm section length of suspension insulator and post insulator respectively. The electric field strength which was particularly extreme at the high voltage end extremities of the insulators is reduced below 3.5 kV/cm.

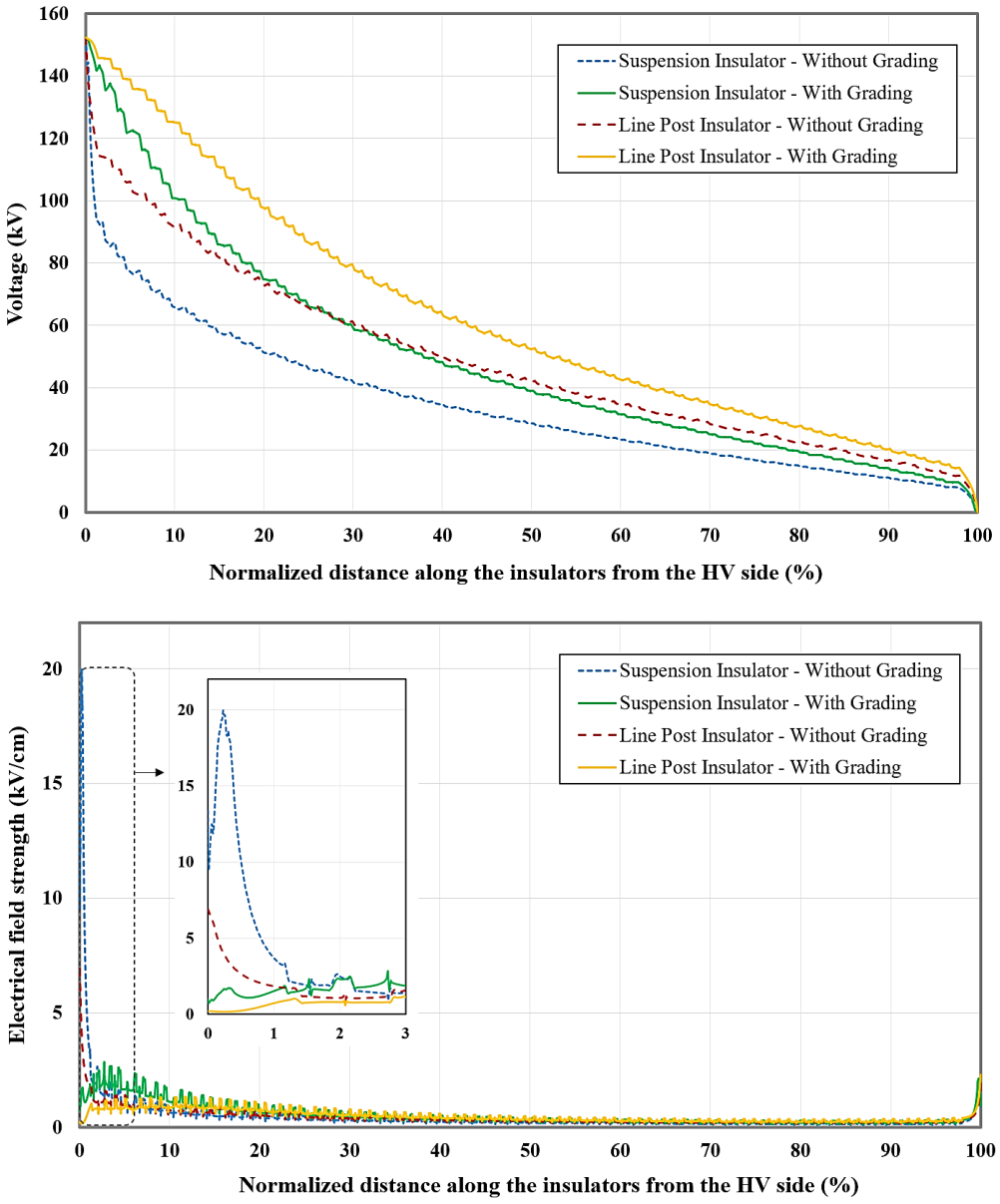

Figure 21. Comparative potential and electric field distribution along composite cross-arm insulator with and without grading devices.

As noted before, the study for optimization of grading devices was carried out by considering the insulated cross-arm retrofitted on the bottom most phases of the transmission tower. Once these design optimizations were completed, electric field simulations were also carried out by considering the insulated cross-arm attached to the middle phase position so as to validate the field grading performance for the situations where all existing steel cross-arms may be retrofitted with this composite insulated cross-arm or when the cross-arm may be applied for a completely new-build compact line.

IV. Single Phase Simulations

Single phase simulations with laboratory test set-up and representative models were performed with an aim to verify and predict the performance of composite insulated cross-arm in full-scale corona extinction voltage and water droplet induced corona tests and also to evaluate the extent of differences in the electric field

distribution on the cross-arm between the service and lab test conditions. The voltage boundary condition used in these single-phase simulations was equal to 1.2*1.1*240/√3 ≅ 183 kV, which is 20% higher than the voltage applied in three phase simulations and corresponds to the minimum specified corona extinction test voltage. Both detailed and simplified representation of the laboratory environment were analyzed.

A. Detailed Laboratory Model

In the detailed laboratory model, the high voltage test hall with a trapezoidal volume of 10/28 x 25 x 42 m was simulated. In addition to the detailed representation of the insulated cross assembly, suspension fittings and the double-cross support structure; the AC transformer, voltage divider, coupling capacitor and the conductor end shielding electrodes were included in the model while other far-away objects in the test hall were ignored. The detailed laboratory simulation model is shown in Figure 22. Mesh and other settings on each component of the insulated cross-arm assembly were kept consistent with the three-phase service simulation model.

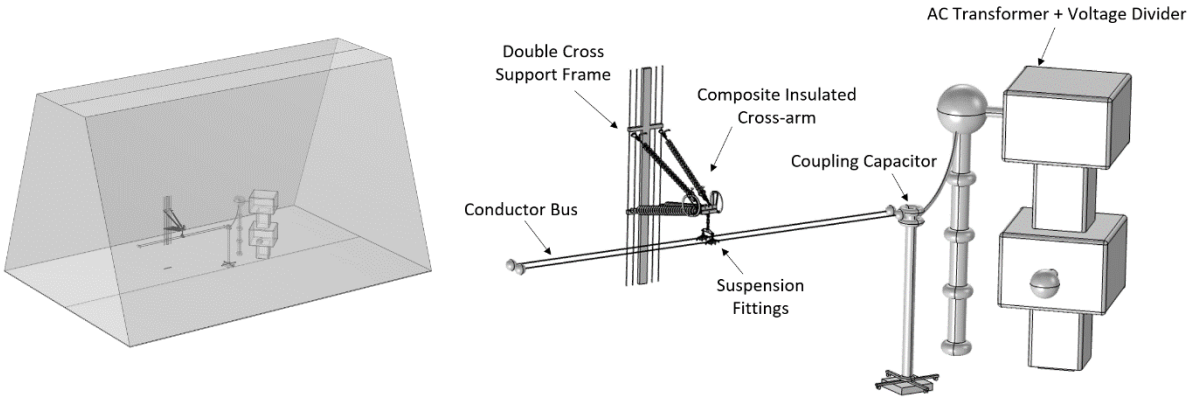

Figure 22. Detailed laboratory simulation model.

B. Simplified Laboratory Model

In the simplified laboratory model, the AC transformer, voltage divider and the coupling capacitor were ignored and the air domain was reduced from the trapezoidal volume representing the full HV laboratory test hall to a cuboid with a volume of 12 x 20 x 20 m as shown in Figure 23. All other details in the simplified model were retained.

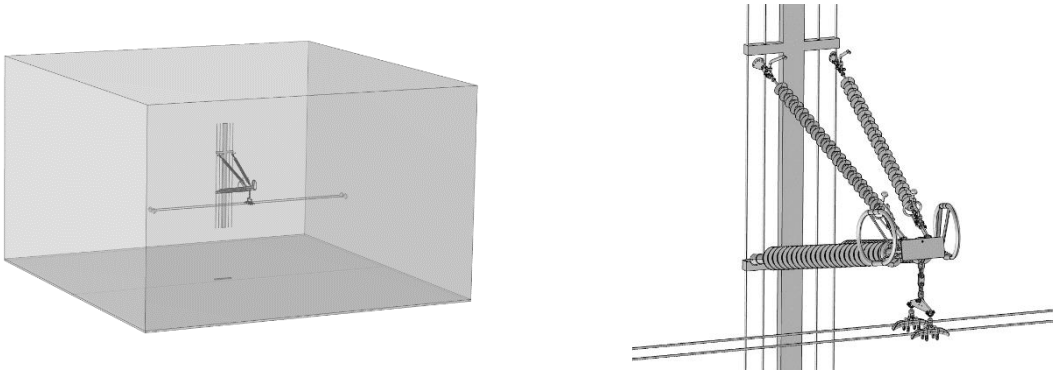

Figure 23. Simplified laboratory simulation model.

C. Summary of Simulation Results and Discussion

Table 5 presents the electric field simulation results on select points for the detailed and simplified single phase model. It can be seen that the calculation results between the two models is quite close with only the field stress on the high voltage grading rings showing a slight increase of about ~ 1% to 2% in the detailed model. Taking into account the small margin of error, ease in building the model as well as lesser computational time - the simplified single phase simulation model is clearly more preferable.

Table 5. Electric field results for single phase laboratory simulation models

Point of Interest	Maximum Electric Field (kV/cm)		% Difference (Simplified-Detailed)
	Detailed Model	Simplified Model	
Suspension insulator housing	3.221	3.222	0.02
Line post insulator housing	1.889	1.890	0.09
Node shielding ring	9.763	9.772	0.09
Line post insulator grading ring	4.957	5.002	0.91
Suspension insulator arcing ring (HV)	15.537	15.320	1.40
Suspension insulator arcing horn (LV)	15.343	15.425	0.53

Ignoring the effects of surface roughness and by considering only the adjustment for relative air density, the corona inception (on-set) gradient for a sphere of 70 mm diameter using Equation 1 [14] is estimated to be approximately 22 kV/cm.

$$E_d = 32.4 \cdot m \cdot \delta \cdot r_{eq}^{-0.3} \quad \text{Eq. 1}$$

Where m is the surface roughness factor, δ is the relative air density factor, E_d is the electrode corona onset gradient and r_{eq} is the equivalent radius of the electrode.

In single-phase laboratory simulations, the highest magnitude of electric field stress was found on the suspension insulator arcing spheres (70 mm diameter) and, on the under-side of circular bolt heads (16 mm diameter) of the conductor suspension clamp with maximum values of 15.54 kV/cm and 20.93 kV/cm respectively. Since these field stresses remain below the minimum estimated corona on-set gradient, the insulated cross-arm was expected to be corona free with an applied test voltage of well above 183 kV. Furthermore, it was anticipated that during actual testing visible corona inception would be observed on the aforementioned two regions. Electric field strength on the insulator housings were also found to be below the prescribed guidelines to avoid water droplet induced corona.

Lastly, it was also considered worthwhile to compare the electric field simulation results of the three-phase and single-phase models. To get the equivalent voltage boundary conditions between two models, the electric field results of single-phase simulation were scaled down by a factor of 1.2 (equivalent to the ratio of 183 kV to 154 kV). On points of interest on the high voltage side of the insulated cross-arm, the electric field in the three-phase model was approximately 19 % higher on metallic hardware and 17 % higher on insulator housings - which can be attributed to the influence of adjacent phases. On the other hand, a more significant difference in the electric field distribution was observed on the low voltage side of the insulated cross-arm which is highlighted in Figure 24. This abrupt increase seen in electric field strength on the low voltage side in the single-phase model is due to the lack of shielding provided by the extended metallic body and middle metal cross-arm of the tower in the three-phase service model. Since the electric fields remained below critical values no further adjustments were made to the test set-up.

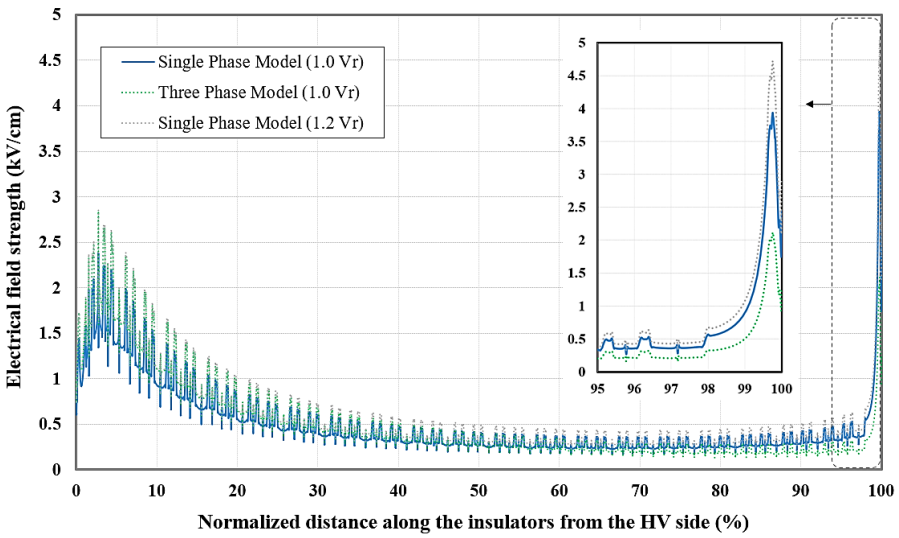

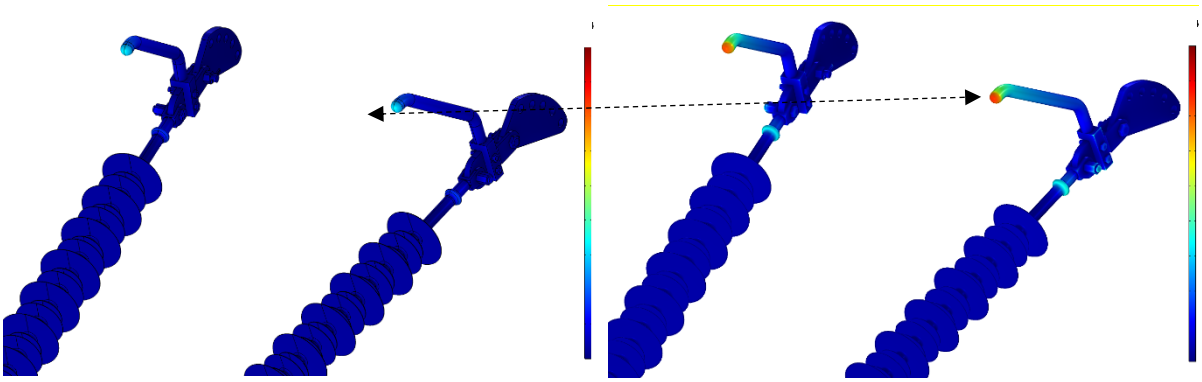

Figure 24. Differences in electric field distribution in the three-phase service model and single-phase model.

V. Laboratory Tests

In order to benchmark the results of electric field simulations and to confirm performance of the designed electric field grading system, the 240 kV composite insulated cross-arm was subjected to corona extinction, radio interference voltage (RIV) and water droplet induced corona (WDIC) tests. The tests were performed in the HV laboratory of EGU in Prague, Czech Republic. A test arrangement close to the actual service conditions was devised. The insulated cross-arm assembly together with conductor suspension fitting string was mounted on a 6 m x 1 m double-cross support structure which simulated the tower body ground plane with metallic tubes displaced 200 mm apart. Conductors were simulated by φ 22 mm aluminum tubes of 12 m length with 457 mm horizontal bundle spacing placed at a height of 4.05 m above the ground. The entire test set-up was suspended by a roof crane and a suitable counter weight was used to keep the assembly up-right as shown in Figure 25.

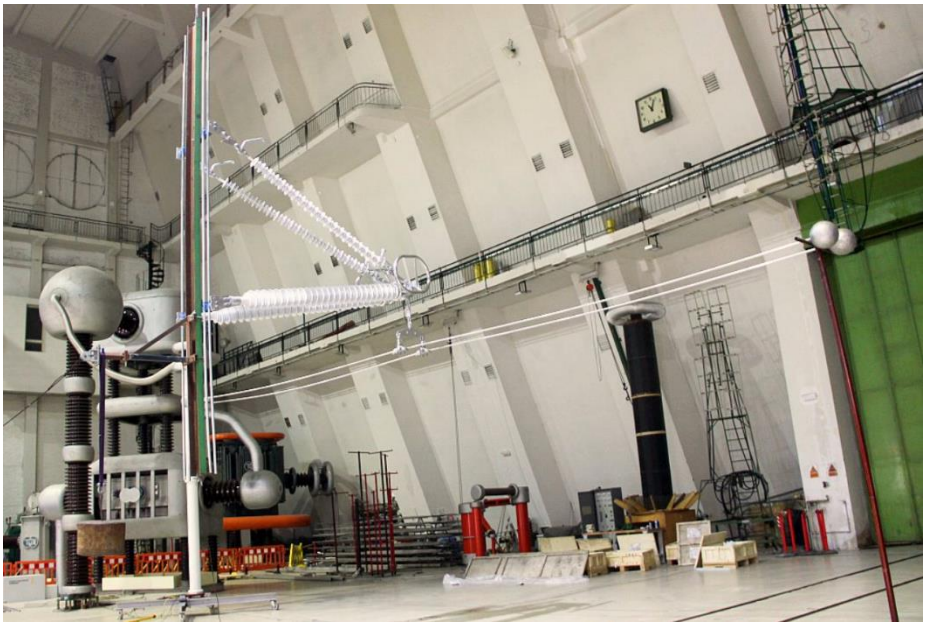

Figure 25. Set-up for corona and RIV tests of composite insulated cross-arm with simulation of the tower body and conductor bundle.

A. Corona Extinction Test

Voltage gradient method according to the procedure described in CSA 411.4 [15] was applied. The gradient method aims to replicate the surface voltage gradient that occurs on the conductors of three-phase transmission lines. A calibration procedure was used to determine the test voltage. Firstly, the required conductor surface voltage gradient (E_2) of 17.25 kV/cm was analytically calculated. E_2 is the mid-span conductor surface gradient based on the actual geometry and design of the transmission line.

A calibrating sphere with a diameter of 3.18 mm was mounted a single φ 22 mm conductor approximately at its mid-point and placed at a height of 0.52 m above the ground as shown in Figure 26. Calibration was performed by increasing the applied voltage to the conductor and observing the positive corona extinction voltage of the sphere. This process was repeated three times and the average value was used to calculate the positive corona inception gradient for conductor-mounted calibration device (E_c) according to Equation 2.

$$E_c = \frac{V}{r \cdot \ln\frac{2h}{r}} \qquad \text{Eq. 2}$$

Where, V is the average positive corona extinction voltage of the sphere, r is the radius of the conductor and h is the height of the test conductor to the ground plane.

Next the calibrating sphere was mounted in the middle of the 12 m long twin conductor bundle supported 4.05 m above the ground as shown in Figure 27. The voltage was raised and the positive corona inception voltage (V_c) was recorded. The results of this calibration procedure are summarized in Table 6 and Table 7.

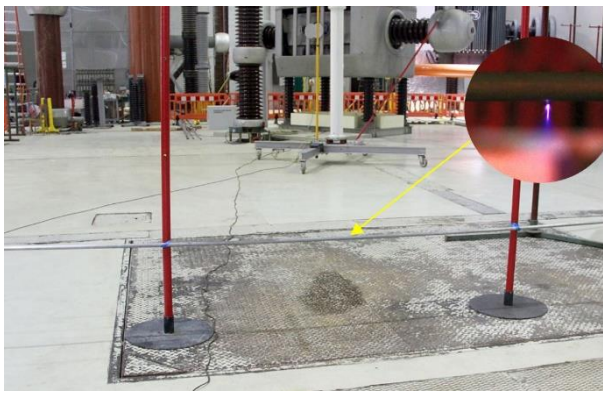

Figure 26. Test arrangement and corona inception on calibration sphere mounted on single conductor.

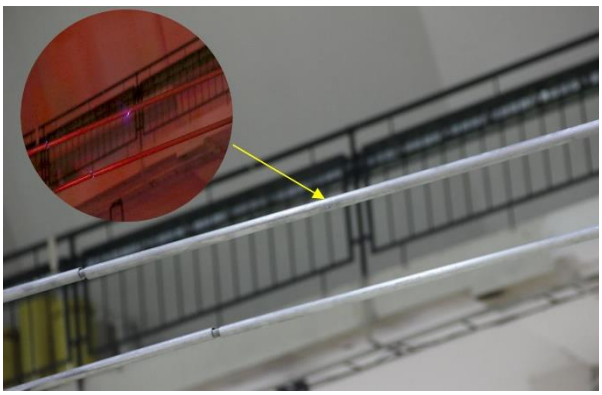

Figure 27. Test arrangement and corona inception on calibration sphere mounted on twin conductor bundle.

Table 6. Calibration results of 3.18 mm sphere on 22 mm single conductor 0.52 m above ground

Positive Corona Extinction Voltage of Calibrating Sphere (kV)			Average (kV)	E_c (kV/cm)
80	83	86	83	16.58

Table 7. Calibration results of 3.18 mm sphere on 22 mm twin bundle conductor 4.05 m above ground

Positive Corona Extinction Voltage of Calibrating Sphere, V_c (kV)			Average (kV)
179	172	178	176

Finally, the required test voltage (V_T) of 220 kV was computed according to Equation 3 where the factor of 1.2 takes into account the reduced air density for high altitude applications and ageing or roughness of surface that occurs due to long exposure to environment in field operation. It is noted that the applied standard [15] states that the test voltage shall be within ± 20% of maximum design phase-to-ground service voltage, which means that the test voltage should be limited to 183 kV. Nonetheless, given the favorable simulation results it was decided to check corona extinction at a test voltage of 220 kV. After the test hall was darkened, a test voltage above the corona inception voltage was applied to the insulated cross-arm assembly and then

gradually decreased to measure the positive corona extinction voltage. Binoculars were used for observation of corona. No positive corona was observed on the cross-arm at a test voltage of 220 kV as shown in Figure 28. The obtained results of the positive corona extinction voltage are in presented in Table 8.

$$V_T = 1.2 \cdot \frac{E_2 \cdot V_c}{E_c} \qquad \text{Eq. 3}$$

Table 8. Results of corona extinction voltage test

Measurement	Positive Corona Extinction Voltage (kV)	
	Arcing sphere	Suspension Clamp
1	278	251
2	282	253
3	283	254
Average	281	253

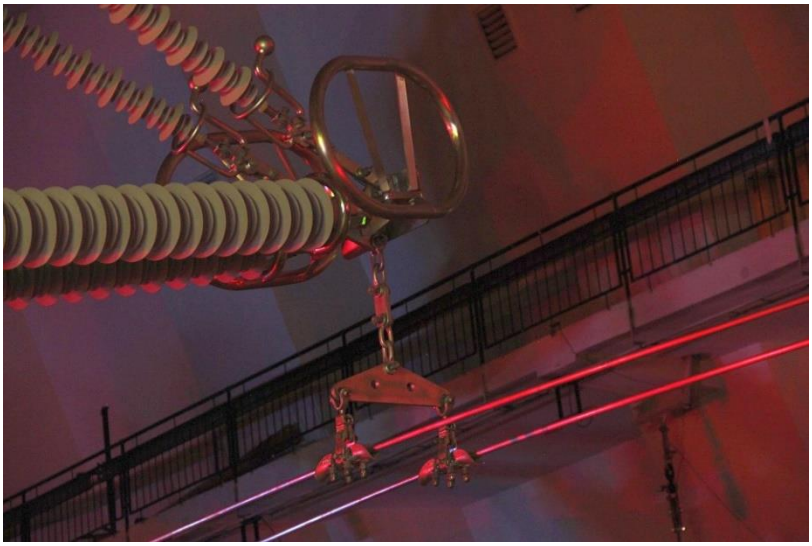

Figure 28. No visible corona at an applied test voltage of 220 kV.

As depicted in Figure 29, corona was mainly visible on the tips of the arcing spheres and the bottom side of the conductor suspension clamps which validates the simulation results.

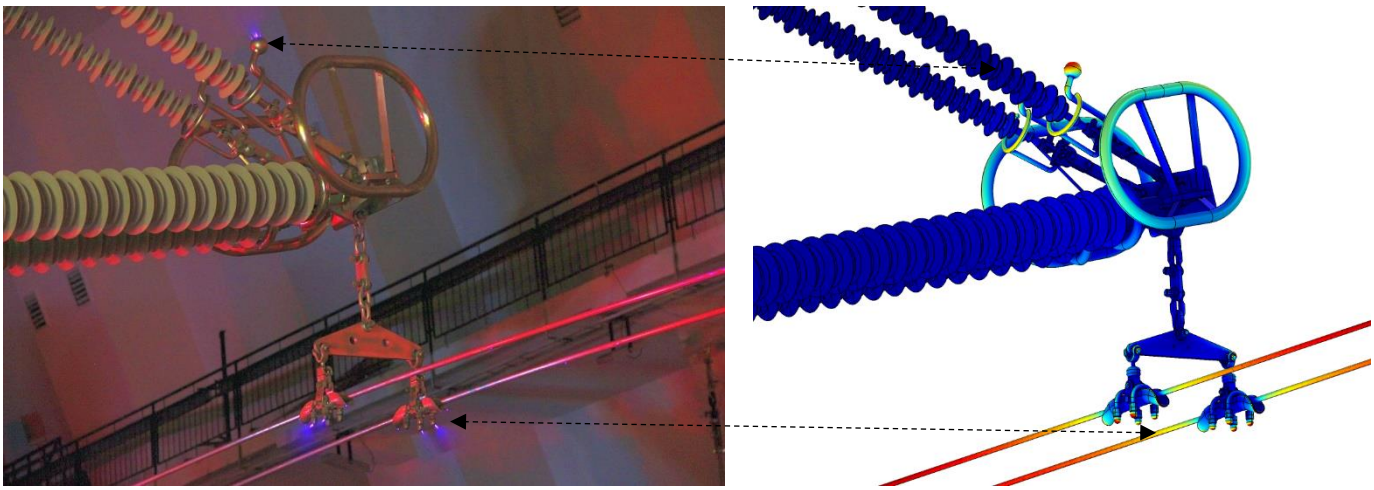

Figure 29. Comparison of corona inception and electric field simulation

B. Radio Interference Voltage Test

The radio inference voltage (RIV) test was carried out according to IEC 60437 [16]. RIV expressed in dB relative to 1µV across 300 Ω was measured at the frequency of 1 MHz. The test set-up and arrangement used was identical to the corona extinction voltage test. Figure 30 presents the obtained RIV characteristics. RIV of 39 dB/1µV was measured at a test voltage of 168 kV which is lower than the acceptance value of 52 dB.

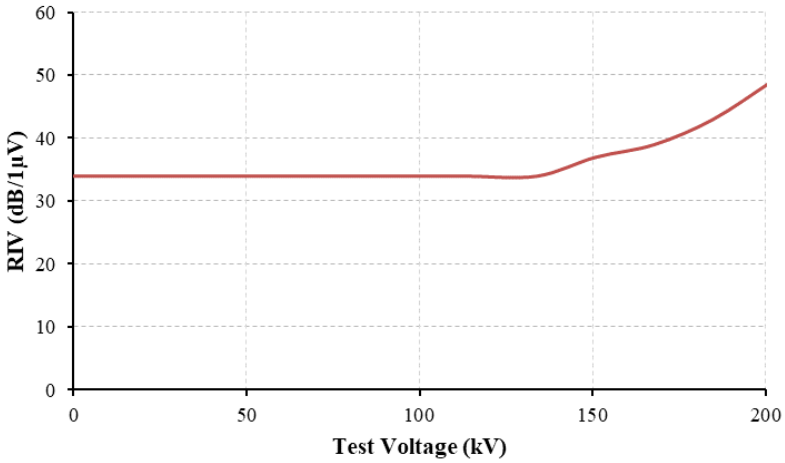

Figure 30. RIV characteristics of the composite insulated cross-arm.

C. Water Droplet Induced Corona Test

While the visible corona extinction and RIV tests have long been used for verifying the electric field stress on metallic hardware of insulator sets, recently the application of water droplet induced corona (WDIC) test has gained popularity which aims to verify the electric field limits on the housing of the composite insulators so that no water droplet corona appears on the insulators in-service. Test method according to the recommendations made in [17] was applied. The test set-up, environment and voltage application are similar to a standard RIV test. Before voltage application, suspension and line post insulators of composite cross-arm were wetted with a spray bottle from a distance of approximately 25 cm for 5 seconds. All metallic parts of the cross-arm were thoroughly dried with a wiping cloth to avoid corona from them. Views of cross-arm insulators during WDIC test are shown in Figure 31. WDIC test required the assembly to be corona free at the rated voltage of system which in this case was equal to $264/\sqrt{3} = 153$ kV. Observation was made with standard photo cameras and no WDIC was observed during the tests.

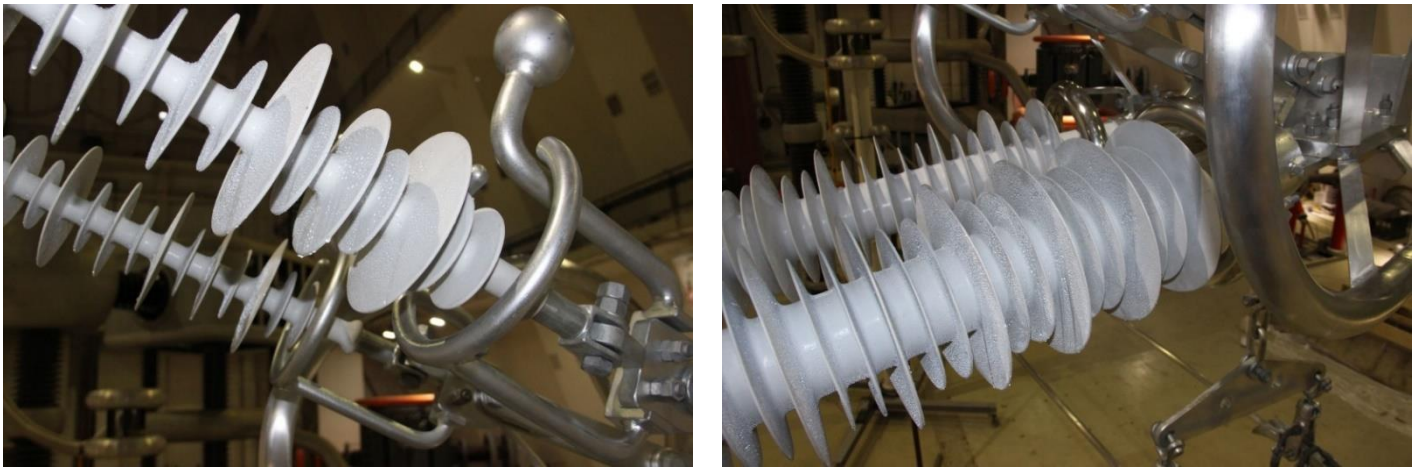

Figure 31. Water droplet induced corona test of insulated cross-arm, left: suspension insulators and right: line post insulators.

VI. Conclusions

Electric field control on composite insulated cross-arms presents some specific challenges and necessitate dedicated grading devices for it's different composite and metallic components, often with competing requirements. The obtained results of the parametric study show that in general, an increase in tube size and outer diameter of grading rings leads to a decrease in electric field stress however, their position with respect to the concerned point of interest needs to be carefully selected to get the optimal results.

For the same voltage boundary condition, three-phase simulation gives higher electric field magnitude on the high voltage side compared to a single-phase simulation, but there can be significant variations in the field distribution on the low voltage side due to differences in size and geometry of the ground planes between the two models. The simplified single-phase model provides a good approximation of the detailed single-phase simulation with a little loss of accuracy.

In addition to ensuring reliable long term field performance, simulations provide a useful tool in predicting laboratory test behavior and expected results. Using the optimized grading devices, the 240 kV composite insulated cross-arm passed the dry and wet corona tests and the RIV test.

VII. References

[1] Paris, L., L. Pargamin, and R. Parraud, "Application of Composite Insulators for Overhead Compact Lines," CIGRE Symposium Leningrad. 1991.

[2] A. J. Phillips, D. J. Childs and H. M. Schneider, "Aging of nonceramic insulators due to corona from water drops," in IEEE Transactions on Power Delivery, vol. 14, no. 3, pp. 1081-1089, July 1999.

[3] Schümann, U., F. Barcikowski, M. Schreiber, H. C. Kärner, and J. M. Seifert, "FEM calculation and measurement of the electrical field distribution of HV composite insulator arrangements," 39th CIGRE Session, 33-404 pp. 1-6. 2002.

[4] C. Zachariades, S. M. Rowland, I. Cotton, V. Peesapati and D. Chambers, "Development of Electric-Field Stress Control Devices for a 132 kV Insulating Cross-Arm Using Finite-Element Analysis," in IEEE Transactions on Power Delivery, vol. 31, no. 5, pp. 2105-2113, Oct. 2016.

[5] X. Yang, N. Li, Z. Peng, J. Liao and Q. Wang, "Potential distribution computation and structure optimization for composite cross-arms in 750 kV AC transmission line," in IEEE Transactions on Dielectrics and Electrical Insulation, vol. 21, no. 4, pp. 1660-1669, August 2014.

[6] P. Sidenvall, I. Gutman, J. Schulte-Fischedick, J. Seifert and J. Goffinet, "Methodology of modern E-field calculations — Case study for insulated cross-arm," 2013 Annual Report Conference on Electrical Insulation and Dielectric Phenomena, 2013, pp. 334-337.

[7] L. Yao-qin, H. Feng and N. Jing, "Test and Simulation Analysis on the Electric Field Distribution Characteristics of UHVAC Composite Cross-arm Fittings," 2019 IEEE Sustainable Power and Energy Conference (iSPEC), 2019, pp. 2905-2910.

[8] P. He, Z. Yu, Q. Yang and B. Zhang, "Design of Grading Ring for Composite Cross-arm in 500 kV Single-Circuit Transmission Tower," 2018 IEEE International Conference on High Voltage Engineering and Application (ICHVE), 2018, pp. 1-4.

[9] Y. Zhu, L. Wang, J. Yu and J. Fang, "Optimal insulation design for new-type transmission tower with composite cross-arm," 2017 International Symposium on Electrical Insulating Materials (ISEIM), 2017, pp. 578-581.

[10] Jialong Wang, Z. Peng, Hao Wu, Hongwei Deng, Hao Liu and Chuang Wang, "Electric field calculation and grading ring design for 330kV terminal tower with composite cross-arms," 2016 IEEE International Conference on Dielectrics (ICD), 2016, pp. 346-349.

[11] Gao Yanfeng, Wu Chao, Liang Xidong, Liu Yingyan, Wang Guoli and Gao Chao, "Electric field and electromagnetic environment analyses of a 500 kV composite cross-arm," 2015 IEEE Conference on Electrical Insulation and Dielectric Phenomena (CEIDP), 2015, pp. 399-402.

[12] Qingyu Wang, Zongren Peng, Xi Yang, Naiyi Li, Jialong Wang and Jintao Liao, "Electric field computation and optimization of composite tower in 330 kV double circuit transmission lines," 2014 IEEE Conference on Electrical Insulation and Dielectric Phenomena (CEIDP), 2014, pp. 283-286.

[13] A. J. Phillips, A. J. Maxwell, C. S. Engelbrecht and I. Gutman, "Electric-Field Limits for the Design of Grading Rings for Composite Line Insulators," in IEEE Transactions on Power Delivery, vol. 30, no. 3, pp. 1110-1118, June 2015.

[14] EPRI AC Transmission Line Reference Book-200 kV and Above, 3rd ed. Palo Alto, CA: Electric Power Research Institute, Dec. 2005.

[15] Composite Suspension Insulators for Transmission Applications, CSA-C411.4, 2008.

[16] Radio interference test on high-voltage insulators, IEC 60437, 1997.

[17] P. Sidenvall, I. Gutman, L. Carlshem, J. Bartsch and R. Kleveborn, "Development of the water drop–induced corona test method for composite insulators," in IEEE Electrical Insulation Magazine, vol. 31, no. 6, pp. 43-51, November-December 2015.